Chemically Resolving Protein Phase Separation with Quantum-Enhanced Picoliter NMR

Mengze Shen[1†], Zhiyuan Zhao[1,2†], Haolin Zhang[1,2], Qiunan Ren[3], Xi Kong[8], Zhiping Yang[1,2,5], Tianyu Xie[1,2], Ke Ruan[1], Shengqi Xiang[1,3*], Fazhan Shi[1,2,4,5,6*], Jiangfeng Du[4,7*]

[1]Laboratory of Spin Magnetic Resonance, School of Physical Sciences, Anhui Province Key Laboratory of Scientific Instrument Development and Application, University of Science and Technology of China, Hefei 230026, China.

[2]Hefei National Research Center for Physical Sciences at the Microscale, University of Science and Technology of China, Hefei 230026, China.

[3]MOE Key Laboratory for Cellular Dynamics, School of Life Sciences, University of Science and Technology of China, Hefei, China.

[4]Hefei National Laboratory, University of Science and Technology of China, Hefei 230088, China.

[5]School of Biomedical Engineering and Suzhou Institute for Advanced Research, University of Science and Technology of China, Suzhou 215123, China.

[6]The First Affiliated Hospital of USTC, Division of Life Sciences and Medicine, University of Science and Technology of China, Hefei 230026, China.

[7]State Key Laboratory of Ocean Sensing and School of Physics, Zhejiang University, Hangzhou 310058, China.

[8]National Laboratory of Solid State Microstructures and Department of Physics, Nanjing University, Nanjing 210093, China.

*Corresponding author. Email: fzshi@ustc.edu.cn, cqxiang@ustc.edu.cn, djf@ustc.edu.cn

†These authors contributed equally to this work.

Biomolecular condensates formed through liquid–liquid phase separation (LLPS) organize essential cellular functions as membraneless organelles. Understanding their internal atomic-level chemistry is critical, but inaccessible to classical nuclear magnetic resonance (NMR) due to their picoliter volumes. While emerging quantum sensing has extended NMR to this scale, applying this capability to chemically resolve biologically significant microenvironments remains a key objective. Here, we introduce a diamond nitrogen-vacancy quantum sensor with a 0.19 ppm resolution in ~12 pL. Enabled by confined-chamber deuteration, protective metallization, and sensitivity enhancement, this platform enabled chemically resolved protein NMR spectra of LLPS condensates, distinguishing protons in distinct structural positions. This work extends atomic-resolution spectroscopy to the subcellular scale, opening a window onto the molecular environments that underlie heterogeneous function at the cell scale.

Cells organize their cytoplasm by forming membraneless organelles, such as P granules, through a process of LLPS (*1*). These biomolecular condensates are critical for fundamental processes ranging from gene regulation and stress response to cellular decision-making (*2–5*). However, a major challenge is to understand the molecular rules that govern their assembly and function at an atomic level. Nuclear Magnetic Resonance (NMR) spectroscopy is uniquely suited to this challenge, as it provides unique insights into the structure, dynamics, and interactions of proteins in their native solution state (*6–8*). Conventional NMR methods have been widely applied to study LLPS systems, yet they are limited to capturing averaged signals in a large ensemble. (*9–15*).

This averaging is problematic because the dynamic and compositionally heterogeneous nature makes each condensate a distinct reaction compartment, underscoring the need to probe individual droplets to understand their internal molecular organization and function. However, detecting NMR signals from a single condensate, which is only a few micrometers in size, remains a formidable challenge. Conventional spectrometers require trillions of molecules at a volume over

10 μL (*16, 17*). While miniaturization efforts such as microcoils NMR have maintained excellent spectral resolution, their typical detection volumes remain too large (>1 nL) for organelle-level investigation (*18–22*). Recently, the optically detected nitrogen-vacancy (NV) center in diamond has been proven as a versatile tool for investigating microscale biological samples (*23–28*). Although protocols have been developed for obtaining NMR information on a nanometer scale (*29–32*) or micrometer scale (*33–35*), existing technologies cannot simultaneously meet the three essential requirements for practical biological investigation: cellular-scale detection volumes, sub-ppm spectral resolution, and the sensitivity to probe unmodified biomolecules in their native state, leaving crucial biological processes at the cellular scale largely inaccessible to NMR analysis.

Here, we bridge this gap and obtain chemically resolved NMR spectra of phase-separated protein condensates by applying a microfluidics-equipped NV-diamond quantum sensing platform that achieves a resolution of 0.19 ± 0.04 ppm within a ~12 pL volume.

To demonstrate this capability, we selected the phenylalanine-glycine-glycine (FGG) repeat region (residues 15-154) of the germ line helicase 1 (GLH-1) protein (hereafter, the protein). As previously reported for FG-repeat regions in other proteins, this FGG region also undergoes LLPS (*36, 37*). As a core component of P granules in C. elegans, this protein is well-characterized for its critical role in defining their material properties (such as soft-to-solid transitions) and ensuring their precise perinuclear anchoring in the germline (*38–40*). By applying our technology to this system, we captured the first chemically resolved spectrum of protein condensation at the picoliter scale. This successful detection of the condensing GLH-1 FGG domain thus serves as a robust validation of our tool's sensitivity and unlocks the potential to chemically resolve biological processes at their native, cellular scale.

A quantum sensing platform for picoliter NMR

Achieving the above goal required us to overcome several fundamental and interconnected challenges systematically: First, we had to address the severe signal-to-noise ratio (SNR) deficit arising from the picoliter-scale detection volume and the low protein concentration. Second, we needed to achieve sub-ppm spectral resolution, a critical prerequisite for resolving the chemical shifts from different components in proteins. Finally, it is necessary to protect sample integrity during long

acquisitions.

Firstly, to improve SNR, our strategy considered both signal enhancement and noise suppression. To enhance the signal, we used a free radical as a polarizing agent and applied Overhauser dynamic nuclear polarization (ODNP), which increased the nuclear spin signal by two orders of magnitude compared to its thermal equilibrium value (*41, 42*). To suppress noise, we engineered an integrated fluorescence collection path using a compound parabolic concentrator (CPC) lens to improve photon collection efficiency (Fig. 1A). Two referencing systems, i.e., a second photodiode and paired readouts, were employed to cancel laser intensity noise and reject common-mode noise from the control electronics, respectively (Fig. 1B). Each data point is calculated by subtracting two consecutive readouts in a paired-readout scheme for common-mode noise rejection. The time interval between the two sub-sequences is set to $(n + 0.5) \times 1/f_{\mathrm{Larmor}}$ to achieve this.

Secondly, achieving high spectral resolution required both an advanced detection protocol and a highly stable, homogeneous magnetic field. We employed a coherently averaged synchronized readout (CASR) pulse sequence (*43–45*) (Fig. 1B), ensuring the resolution was not limited by the NV center coherence time. To maintain field stability, even in a standard, unshielded urban laboratory, we engineered a robust environment combining a temperature-stabilized, shimmed permanent magnet with an active dual-mode feedback system and carefully selected non-magnetic materials near the sensor to minimize local field distortions (Supplementary Text).

Thirdly, the final challenge of sample integrity was addressed through several approaches. Samples were delivered via an integrated microfluidic channel, isolating them from the open air and reducing the sensor perturbation during sample injection. To prevent laser-induced heating, we used an epifluorescence geometry and fabricated a patterned Ti/Ag/Al reflective film on the diamond surface using a PDMS shadow mask. The sample was effectively protected from the laser, while the patterned film minimized the effects on the microwave field. To mitigate potential microwave heating, a conservative duty cycle of approximately 4 s per shot was implemented, preserving the native state of the temperature-sensitive LLPS droplets.

By measuring the proton signal from water, we clearly observed the nuclear spin Larmor precession in the time domain (Fig. 1, C and D) and obtained the sharp spectrum shown in Fig. 1E through Fourier transformation. A Lorentzian fit reveals a narrow linewidth of 0.98 ± 0.21 Hz, or 0.19 ± 0.04 ppm. To further improve the signal-to-noise ratio, we performed averaging over 100

measurements. Although this introduces a slight broadening due to residual magnetic field drifts (1.49 Hz or 0.29 ppm, Fig. 1F), the resolution remains well within the sub-ppm regime required for resolving protein chemical shifts. This result confirms that our platform has the fundamental capabilities needed for high-resolution biomolecular NMR.

(Fig. 1G) benchmarks our platform against state-of-the-art micro-scale NMR techniques. Our platform occupies a distinct regime, achieving a spectral resolution of 0.19 ppm from a sensing volume of approximately 12 pL (equivalent to a 30 μm diameter sphere). This combination allows us to detect NMR signals from proteins within micrometer-sized droplets represents a significant breakthrough in bridging the gap between structural biology and cell biology. Due to the inherent dynamics and heterogeneity of membraneless organelles, this capability to directly observe individual condensates carries profound physiological significance.

Chemically-resolved spectroscopy of protein condensates

To isolate weak protein signals from the overwhelming solvent background, we first established a rigorous experimental logic to ensure measurement reliability (Fig. 2). Following the optimization experiments in Fig. 1, the microfluidics chamber inevitably retains H_2O (Fig. 2A). By thoroughly flushing the system with 99.9% deuterium oxide (D_2O) until the proton signal is suppressed to the noise floor (Fig. 2B), we verify a clean background for detection. Following this, the injection of the protein sample yields a distinct spectrum (Fig. 2C). The sample was prepared by lyophilization to remove H_2O in the original buffer and subsequently reconstituted in D_2O to prepare the final solution. Crucially, a final flush with D_2O eliminates this signal (Fig. 2D). This reversibility confirms that any detected signal originates exclusively from the sample delivered via the channel, rather than system artifacts. Guided by this validated experimental logic, we applied the workflow to investigate the GLH-1 FGG protein under phase-separating conditions. The sample was prepared by re-dissolving 10 mg of lyophilized protein in 0.3 mL D_2O (final concentration ~2.6 mM). At this concentration, the solution spontaneously undergoes LLPS.

This sample, containing pre-formed protein droplets, was introduced into the microfluidic channel for NMR measurements (Fig. 3A). By monitoring the sample using the established protocol, we observed a distinct time dependence in the protein signal (Fig. 3B). Initially, the protein sig-

nal was below the noise floor. However, in the subsequent measurement, a well-resolved spectrum emerged. This observation strongly suggests a dynamic process that leads to an increase in the protein's concentration within the sensing region over time. A plausible mechanism consistent with this observation is the gradual settling of denser, protein-rich condensates, which are expected to form from the protein solution via LLPS. As these condensates accumulate on the diamond sensor surface, a transition from an undetectable signal (dilute phase) to a clearly resolved spectrum (condensed phase) occurred.

Since the sequence is highly enriched in Glycine (52.9%), Serine (14.3%), Phenylalanine (10.7%), and Asparagine (5.0%) (Fig. 3A), the resulting high-resolution NV-NMR spectrum is dominated by two prominent signal clusters in the aliphatic region (Fig. 3B, bottom). The peak centered at 3.8 ppm is a composite signal primarily from the two most abundant residues (Hα of Glycine and Hβ of Serine). Another peak at 3.05 ppm comes mainly from Hβ of Phenylalanine, Asparagine, and the side-chain protons of other residues. The feature observed around 4.7 ppm comes from the residual water (HDO) peak. The low intensity of this HDO peak, relative to the concentrated protein signals, is consistent with the extensive solvent deuteration performed during sample preparation. Crucially, to verify these assignments, we compared our picoliter-scale spectrum with a reference spectrum obtained via conventional 600 MHz NMR on a bulk sample (Fig. 3C). Although the low-field regime introduces strong coupling effects, the lack of scalar coupling between the dominant glycine α-protons and the side-chain protons preserves the distinct separation of these signal clusters (see Supplementary Text). When the high-resolution reference (light blue) is broadened to match the linewidth of our NV sensor (dark blue), the relative positions and overall pattern of these prominent signal clusters show strong agreement with the reference spectrum. This correspondence serves as a robust validation, confirming that our platform accurately reports the chemical "fingerprint" of the protein within the condensates.

Interestingly, the prominent composite feature observed around 3.8 ppm in the condensed phase appears shifted upfield (to lower ppm) compared to the conventional NMR reference. We attribute this apparent shift to differential signal broadening rather than a change in chemical structure. In the condensed phase, the restricted molecular mobility enhances the paramagnetic relaxation enhancement (PRE) effect driven by the free radicals (TEMPOL) in the solution (*46*). Specifically, protons located in structurally rigid positions (such as those Gly Hα near the peptide backbone) experience

faster relaxation and more severe line broadening than those in more flexible environments (such as side-chains). This nonuniform intensity loss causes the spectral weight of the composite peak to tilt towards the side-chain frequencies, resulting in the observed upfield shift of the peak center. While a definitive assignment requires further investigation, an alternative possibility that cannot be fully excluded is that this change also reflects altered local conformations, such as the formation of transient secondary structures (*47, 48*).

To estimate the absolute number of detected molecules, we can model the sensing volume (~12 pL) as being occupied by the condensed phase, which has an estimated local protein concentration of ~35 mM. Under this assumption, the observed signal corresponds to approximately 2.4×10^{11} (420 femtomoles) of protein molecules. This demonstrates a sensitivity regime capable of probing nanogram-level biomolecular assemblies.

In conclusion, we report the first picoliter-scale chemically resolved NMR spectrum of protein condensates, a direct observation of molecular chemical shifts in such a confined biological system. This result was enabled by a key technical advance: achieving, for the first time, sub-ppm spectral resolution at the picoliter scale. Together, these achievements validate our NV-diamond platform as an effective tool for probing biological systems at their native scales.

Discussion and outlook

Looking ahead, the capabilities of our platform can be further improved by focusing on spectral resolution and sensitivity. The resolution could be significantly enhanced by integrating superconducting magnets for higher field strength and stability, along with advanced gradient shimming (*49*) and materials engineering to minimize magnetic susceptibility mismatch (*50, 51*). Beyond improving homogeneity, the integration of pulse field gradients is a critical step toward multidimensional NMR. While the current 1D spectroscopy in D_2O successfully resolves the chemical shift of protons closer to the rigid main chain and those in the flexible side chain, it inherently precludes the observation of exchangeable amide protons, which are the key reporters of protein secondary structure. Future implementation of 2D homonuclear or heteronuclear correlation spectroscopy (e.g., TOCSY or HSQC) will be essential to recover this structural information, disentangle spectral overlap, and fully resolve conformational heterogeneity within individual condensates. In addition, there could

be substantial improvement in sensitivity through several validated techniques. These include leveraging NV-NMR protocols under large field (*52*), incorporating advanced hyperpolarization methods such as parahydrogenation (*53*), and further optimizing both the sample geometry (*54*) and the intrinsic magnetic sensitivity of the NV centers (*23, 55, 56*).

Beyond these established pathways, novel quantum control techniques offer further avenues for enhancement. For example, recently proposed Hamiltonian engineering and AI search sequences could be used to improve the coherence of NV; with proper transferring, the sensitivity of the NV sensor could be further improved (*57, 58*). Regarding spatial resolution, applying these protein preparation protocols to shallow NV centers coupled with nearby nuclear memory qubits could push detection from the picoliter to the nanoscale regime. This roadmap positions NV-based NMR as a promising tool for cell-scale biology, ultimately enabling the in situ observation of metabolic fluxes.

While the ultimate goal is to apply this technology within single living cells, we acknowledge that significant challenges remain, such as signal interference from the complex intracellular environment. Nevertheless, our work represents a critical first step. This work opens a new window for cell biology, extending cellular observation beyond the visible spectrum into the microwave and radio-frequency domains. It preserves spatial distribution information while enabling observations under near-native conditions, providing access to chemical composition, molecular conformation, intermolecular interactions, and dynamic behavior. This progress establishes a critical foundation for future in-situ investigations aimed at achieving a quantitative and structure-resolved understanding of biomolecular behavior in physiological and pathological contexts.

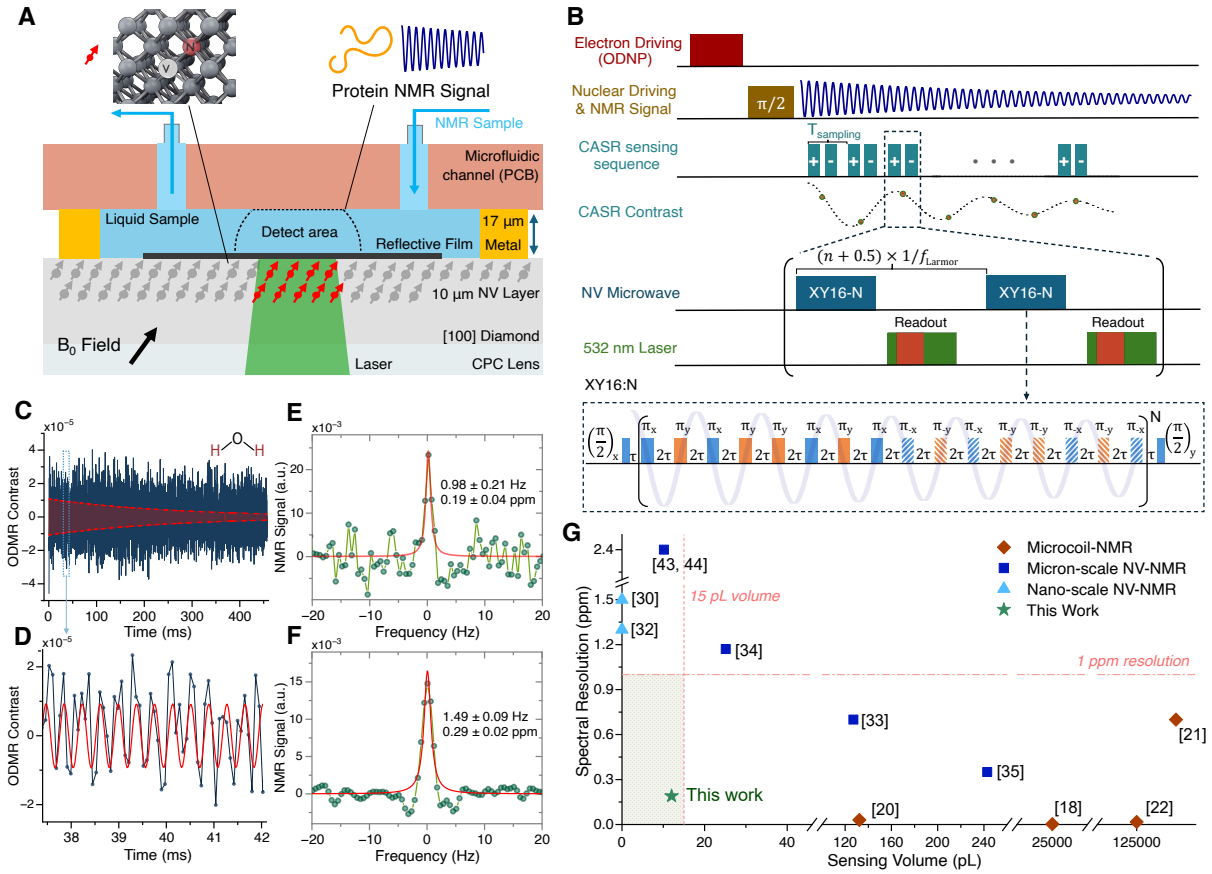

Figure 1: **High-resolution NMR spectroscopy at the picoliter scale.** (**A**) Schematic of the experimental setup. A microfluidic channel integrated with a diamond NV sensor defines a detection volume of ~12 pL. A laser and compound parabolic concentrator (CPC) lens are used for optical spin polarization and readout. (**B**) NV-NMR pulse sequence integrated with Overhauser dynamic nuclear polarization (ODNP) for signal enhancement and coherently averaged synchronized readout (CASR) for detection with paired readouts for common-mode noise rejection. (**C** and **D**) Experimental time-domain ^{1}H NMR signal. (**C**) The signal averaged over 100 scans shows high SNR. (**D**) Zoom-in of time-domain data, showing clear Larmor precession. (**E** and **F**) ^{1}H NMR spectra of water. (**E**) A single-shot spectrum revealing a linewidth of 0.98 ± 0.21 Hz (0.19 ± 0.04 ppm). (**F**) A spectrum averaged over 100 scans with a linewidth of 1.49 ± 0.09 Hz (0.29 ± 0.02 ppm). (**G**) Benchmarking of spectral resolution versus sensing volume for state-of-the-art micro-scale NMR techniques. The dashed lines indicate the upper bound volume of a single mammalian cell (~15 pL) and the spectral resolution required to resolve major metabolites (~1 ppm). The shaded area highlights the requirement for single-cell metabolomics. Our work (green star) occupies a regime previously inaccessible for microscale NMR.

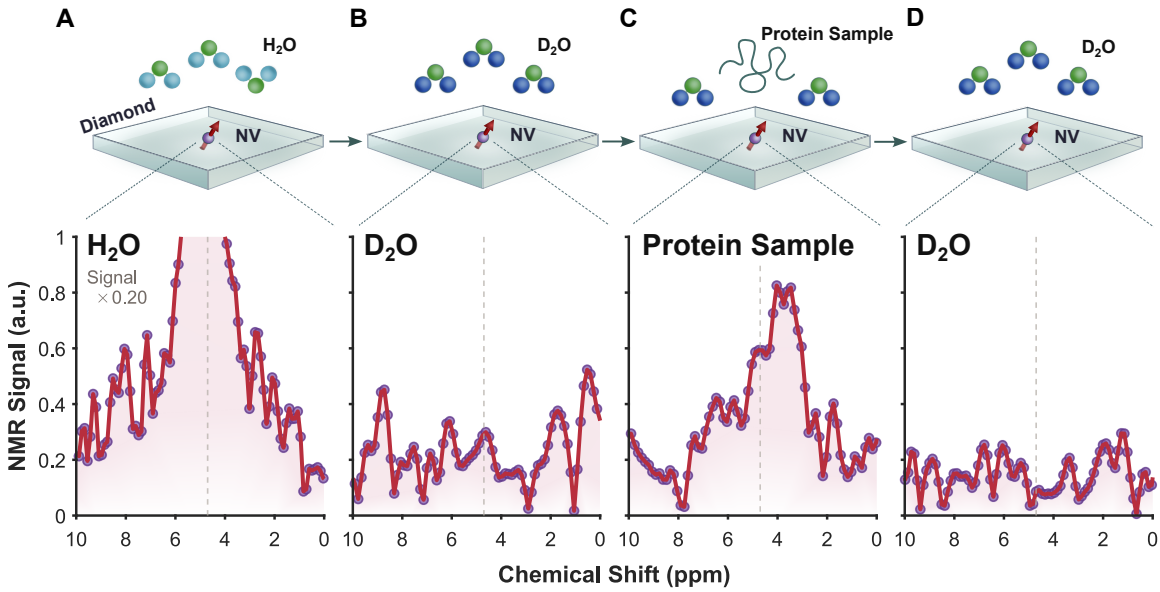

Figure 2: **Validation of NMR signal specificity via microfluidic solvent exchange.** A stepwise sample loading protocol monitored by the NV sensor to ensure signal integrity. Purple circles represent experimental data points, connected by red lines. (**A**) The channel is initially filled with H_2O, yielding a strong proton signal used for setup optimization. (**B**) Flushing with deuterium oxide (D_2O) suppresses the proton signal to the noise floor, confirming a clean magnetic background free from residual solvent. (**C**) Injection of the protein sample (GLH-1 FGG in D_2O) reveals a distinct spectral signature attributed to the protein. (**D**) Subsequent flushing with D_2O eliminates the signal, verifying that the spectrum in (**C**) originates exclusively from the protein sample.

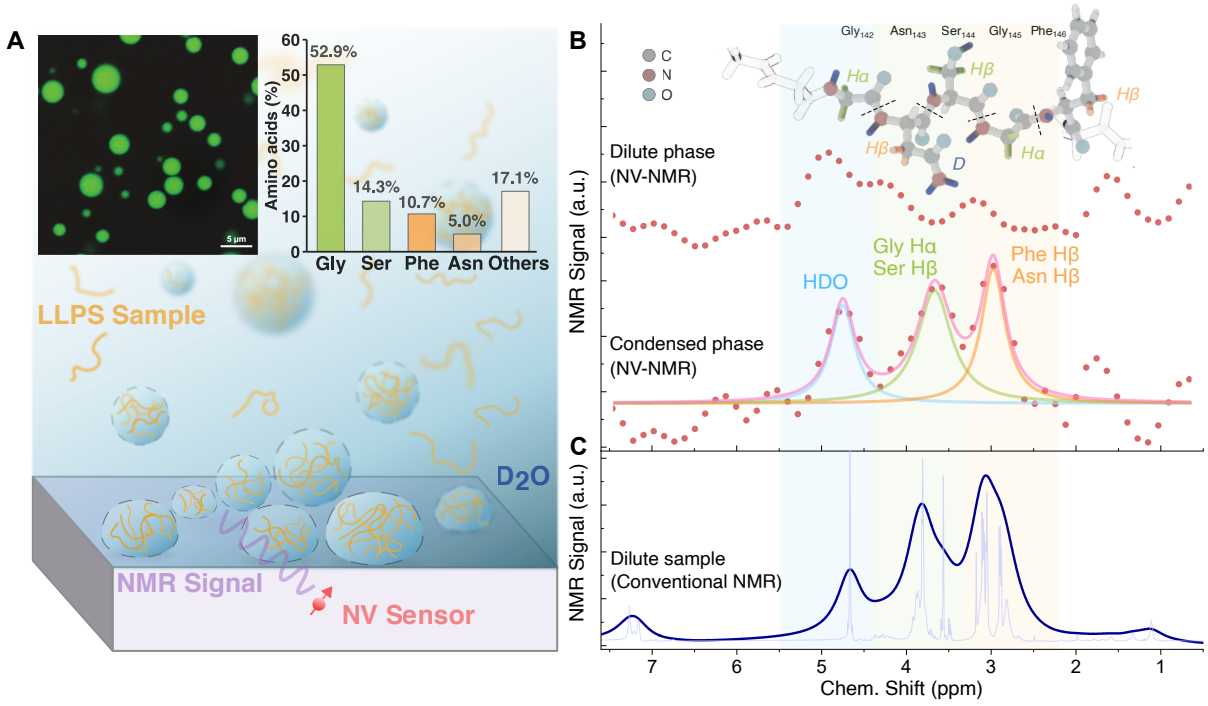

Figure 3: **NV-NMR spectroscopy of GLH-1 FGG condensates.** (**A**) Schematic illustration of liquid-liquid phase separation (LLPS). Protein condensates form from the dilute D_2O solution and settle on the NV sensor surface, enabling detection. Top left inset: Fluorescence image of GLH-1 FGG droplets. Top right inset: Amino acid composition (bar chart) showing the abundance of Glycine (Gly), Serine (Ser), Phenylalanine (Phe), and Asparagine (Asn). (**B**) NV-NMR spectra of the protein. The top trace was initially below the noise floor when there was dilute phase protein in the sensing region. The bottom trace shows a chemically resolved spectrum that emerges upon droplet accumulation on the diamond surface. Solid lines indicate Lorentzian fits for residual solvent (HDO, blue), green cluster from Hα of Gly and Hβ of Ser, and orange cluster from Hβ of Phe, Hβ of Asn, and other side chains. Inset: A representative peptide fragment (Gly_{142}-Phe_{146}, GNSGF) showing the structural origin of the signals. Protons are color-coded as green and orange to match the spectral clusters. (**C**) Validation using conventional NMR. A 600 MHz ^{1}H NMR spectrum of the bulk sample (dark blue line, broadened to match the NV-NMR linewidth) shows good agreement with the NV-detected spectrum, confirming the chemical shift assignments.

References and Notes

1. C. P. Brangwynne, *et al.*, Germline P Granules Are Liquid Droplets That Localize by Controlled Dissolution/Condensation. *Science* **324** (5935), 1729–1732 (2009), doi:10.1126/science.1172046, https://www.science.org/doi/10.1126/science.1172046.

2. S. F. Banani, H. O. Lee, A. A. Hyman, M. K. Rosen, Biomolecular condensates: organizers of cellular biochemistry. *Nature Reviews Molecular Cell Biology* **18** (5), 285–298 (2017), doi:10.1038/nrm.2017.7, https://www.nature.com/articles/nrm.2017.7.

3. Y. Shin, C. P. Brangwynne, Liquid phase condensation in cell physiology and disease. *Science* **357** (6357), eaaf4382 (2017), doi:10.1126/science.aaf4382, https://www.science.org/doi/10.1126/science.aaf4382.

4. X. Su, *et al.*, Phase separation of signaling molecules promotes T cell receptor signal transduction. *Science* **352** (6285), 595–599 (2016), doi:10.1126/science.aad9964, https://www.science.org/doi/10.1126/science.aad9964.

5. P. Li, *et al.*, Phase transitions in the assembly of multivalent signalling proteins. *Nature* **483** (7389), 336–340 (2012), doi:10.1038/nature10879, https://www.nature.com/articles/nature10879.

6. A. Bax, G. M. Clore, Protein NMR: Boundless opportunities. *Journal of Magnetic Resonance* **306**, 187–191 (2019), publisher: Elsevier BV, doi:10.1016/j.jmr.2019.07.037, https://linkinghub.elsevier.com/retrieve/pii/S1090780719301508.

7. Y. Hu, *et al.*, NMR-Based Methods for Protein Analysis. *Analytical Chemistry* **93** (4), 1866–1879 (2021), publisher: American Chemical Society (ACS), doi:10.1021/acs.analchem.0c03830, https://pubs.acs.org/doi/10.1021/acs.analchem.0c03830.

8. A. Sekhar, L. E. Kay, An NMR View of Protein Dynamics in Health and Disease. *Annual Review of Biophysics* **48** (1), 297–319 (2019), doi:10.1146/annurev-biophys-052118-115647, https://www.annualreviews.org/doi/10.1146/annurev-biophys-052118-115647.

9. L. E. Wong, T. H. Kim, D. R. Muhandiram, J. D. Forman-Kay, L. E. Kay, NMR Experiments for Studies of Dilute and Condensed Protein Phases: Application to the Phase-Separating Protein CAPRIN1. *Journal of the American Chemical Society* **142** (5), 2471–2489 (2020), doi:10.1021/jacs.9b12208, https://pubs.acs.org/doi/10.1021/jacs.9b12208.

10. J. E. Bramham, A. P. Golovanov, Temporal and spatial characterisation of protein liquid-liquid phase separation using NMR spectroscopy. *Nature Communications* **13** (1), 1767 (2022), doi:10.1038/s41467-022-29408-z, https://www.nature.com/articles/s41467-022-29408-z.

11. J. P. Brady, *et al.*, Structural and hydrodynamic properties of an intrinsically disordered region of a germ cell-specific protein on phase separation. *Proceedings of the National Academy of Sciences* **114** (39) (2017), doi:10.1073/pnas.1706197114, https://pnas.org/doi/full/10.1073/pnas.1706197114.

12. S. Guseva, *et al.*, Liquid–Liquid Phase Separation Modifies the Dynamic Properties of Intrinsically Disordered Proteins. *Journal of the American Chemical Society* **145** (19), 10548–10563 (2023), publisher: American Chemical Society, doi:10.1021/jacs.2c13647, https://doi.org/10.1021/jacs.2c13647.

13. T. Zeng, J. Li, C. Shi, S. Xiang, Characterization of intrinsically disordered regions through scalar coupling-based solid-state NMR experiments. *Biophysics Reports* **11** (4), 232 (2025), doi:10.52601/bpr.2025.240065, https://www.biophysics-reports.org/article/doi/10.52601/bpr.2025.240065.

14. Q. Ren, *et al.*, The molecular mechanism of temperature-dependent phase separation of heat shock factor 1. *Nature Chemical Biology* **21** (6), 831–842 (2025), doi:10.1038/s41589-024-01806-y, https://www.nature.com/articles/s41589-024-01806-y.

15. Z. Jiang, *et al.*, Crucial role of the cGAS N terminus in mediating flowable and functional cGAS–DNA condensate formation via DNA interactions. *Proceedings of the National Academy of Sciences* **122** (3), e2411659122 (2025), doi:10.1073/pnas.2411659122, https://pnas.org/doi/10.1073/pnas.2411659122.

16. J. Ardenkjaer-Larsen, *et al.*, Facing and Overcoming Sensitivity Challenges in Biomolecular NMR Spectroscopy. *Angewandte Chemie International Edition* **54** (32), 9162–9185 (2015), publisher: Wiley, doi:10.1002/anie.201410653, https://onlinelibrary.wiley.com/doi/10.1002/anie.201410653.

17. F.-X. Theillet, E. Luchinat, In-cell NMR: Why and how? *Progress in Nuclear Magnetic Resonance Spectroscopy* **132-133**, 1–112 (2022), doi:10.1016/j.pnmrs.2022.04.002, https://linkinghub.elsevier.com/retrieve/pii/S0079656522000164.

18. R. M. Fratila, M. V. Gomez, S. Sýkora, A. H. Velders, Multinuclear nanoliter one-dimensional and two-dimensional NMR spectroscopy with a single non-resonant microcoil. *Nature Communications* **5** (1), 3025 (2014), doi:10.1038/ncomms4025, https://www.nature.com/articles/ncomms4025.

19. B. Sequeira-Antunes, H. A. Ferreira, μ-NMR Technology for Biomedical Applications: A Review. *Chemosensors* **12** (12), 248 (2024), publisher: MDPI AG, doi:10.3390/chemosensors12120248, https://www.mdpi.com/2227-9040/12/12/248.

20. M. Grisi, *et al.*, NMR spectroscopy of single sub-nL ova with inductive ultra-compact single-chip probes. *Scientific Reports* **7** (1), 44670 (2017), doi:10.1038/srep44670, https://www.nature.com/articles/srep44670.

21. S. Z. Kiss, N. MacKinnon, J. G. Korvink, Microfluidic Overhauser DNP chip for signal-enhanced compact NMR. *Scientific Reports* **11** (1), 4671 (2021), doi:10.1038/s41598-021-83625-y, https://www.nature.com/articles/s41598-021-83625-y.

22. H. Davoodi, *et al.*, Untuned broadband spiral micro-coils achieve sensitive multi-nuclear NMR TX/RX from microfluidic samples. *Scientific Reports* **11** (1), 7798 (2021), doi:10.1038/s41598-021-87247-2, https://www.nature.com/articles/s41598-021-87247-2.

23. J. F. Barry, *et al.*, Sensitivity optimization for NV-diamond magnetometry. *Reviews of Modern Physics* **92** (1), 015004 (2020), doi:10.1103/RevModPhys.92.015004, https://link.aps.org/doi/10.1103/RevModPhys.92.015004.

24. J. Du, F. Shi, X. Kong, F. Jelezko, J. Wrachtrup, Single-molecule scale magnetic resonance spectroscopy using quantum diamond sensors. *Reviews of Modern Physics* **96** (2), 025001 (2024), doi:10.1103/RevModPhys.96.025001, https://link.aps.org/doi/10.1103/RevModPhys.96.025001.

25. F. Shi, *et al.*, Single-protein spin resonance spectroscopy under ambient conditions. *Science* **347** (6226), 1135–1138 (2015), publisher: American Association for the Advancement of Science (AAAS), doi:10.1126/science.aaa2253, https://www.science.org/doi/10.1126/science.aaa2253.

26. I. Lovchinsky, *et al.*, Nuclear magnetic resonance detection and spectroscopy of single proteins using quantum logic. *Science* **351** (6275), 836–841 (2016), publisher: American Association for the Advancement of Science (AAAS), doi:10.1126/science.aad8022, https://www.science.org/doi/10.1126/science.aad8022.

27. F. Shi, *et al.*, Single-DNA electron spin resonance spectroscopy in aqueous solutions. *Nature Methods* **15** (9), 697–699 (2018), doi:10.1038/s41592-018-0084-1, https://www.nature.com/articles/s41592-018-0084-1.

28. D. R. Glenn, *et al.*, Single-cell magnetic imaging using a quantum diamond microscope. *Nature Methods* **12** (8), 736–738 (2015), doi:10.1038/nmeth.3449, https://www.nature.com/articles/nmeth.3449.

29. N. Aslam, *et al.*, Nanoscale nuclear magnetic resonance with chemical resolution. *Science* **357** (6346), 67–71 (2017), publisher: American Association for the Advancement of Science (AAAS), doi:10.1126/science.aam8697, https://www.science.org/doi/10.1126/science.aam8697.

30. Z. Yang, *et al.*, Detection of magnetic dipolar coupling of water molecules at the nanoscale using quantum magnetometry. *Physical Review B* **97** (20), 205438 (2018), doi:10.1103/PhysRevB.97.205438, https://link.aps.org/doi/10.1103/PhysRevB.97.205438.

31. K. S. Liu, *et al.*, Surface NMR using quantum sensors in diamond. *Proceedings of the National Academy of Sciences* **119** (5), e2111607119 (2022), doi:10.1073/pnas.2111607119, https://pnas.org/doi/full/10.1073/pnas.2111607119.

32. N. R. v. Grafenstein, K. D. Briegel, J. Casanova, D. B. Bucher, Coherent signal detection in the statistical polarization regime enables high-resolution nanoscale NMR spectroscopy (2025), doi:10.48550/arXiv.2501.02093, http://arxiv.org/abs/2501.02093, arXiv:2501.02093 [physics].

33. R. D. Allert, *et al.*, Microfluidic quantum sensing platform for lab-on-a-chip applications. *Lab on a Chip* **22** (24), 4831–4840 (2022), doi:10.1039/D2LC00874B, https://xlink.rsc.org/?DOI=D2LC00874B.

34. J. Smits, *et al.*, Two-dimensional nuclear magnetic resonance spectroscopy with a microfluidic diamond quantum sensor. *Science Advances* **5** (7), eaaw7895 (2019), doi:10.1126/sciadv.aaw7895, https://www.science.org/doi/10.1126/sciadv.aaw7895.

35. J. Smits, *et al.*, Chemically resolved nuclear magnetic resonance spectroscopy by longitudinal magnetization detection with a diamond magnetometer (2025), doi:10.48550/arXiv.2503.02140, http://arxiv.org/abs/2503.02140, arXiv:2503.02140 [physics].

36. S. Frey, D. Görlich, A Saturated FG-Repeat Hydrogel Can Reproduce the Permeability Properties of Nuclear Pore Complexes. *Cell* **130** (3), 512–523 (2007), doi:10.1016/j.cell.2007.06.024, https://linkinghub.elsevier.com/retrieve/pii/S009286740700791X.

37. G. Celetti, *et al.*, The liquid state of FG-nucleoporins mimics permeability barrier properties of nuclear pore complexes. *Journal of Cell Biology* **219** (1), e201907157 (2020), doi:10.1083/jcb.201907157, https://rupress.org/jcb/article/219/1/e201907157/132498/The-liquid-state-of-FG-nucleoporins-mimics.

38. M. Gruidl, *et al.*, Multiple potential germ-line helicases are components of the germ-line-specific P granules of *Caenorhabditis elegans*. *Proceedings of the National Academy of Sciences* **93** (24), 13837–13842 (1996), doi:10.1073/pnas.93.24.13837, https://pnas.org/doi/full/10.1073/pnas.93.24.13837.

39. A. Putnam, M. Cassani, J. Smith, G. Seydoux, A gel phase promotes condensation of liquid P granules in Caenorhabditis elegans embryos. *Nature Structural & Molecular Biology* **26** (3), 220–226 (2019), doi:10.1038/s41594-019-0193-2, https://www.nature.com/articles/s41594-019-0193-2.

40. W. Chen, *et al.*, The Dynamics of P Granule Liquid Droplets Are Regulated by the *Caenorhabditis elegans* Germline RNA Helicase GLH-1 via Its ATP Hydrolysis Cycle. *Genetics* **215** (2), 421–434 (2020), doi:10.1534/genetics.120.303052, https://academic.oup.com/genetics/article/215/2/421/5930420.

41. F. A. L. Anet, A. J. R. Bourn, Nuclear Magnetic Resonance Spectral Assignments from Nuclear Overhauser Effects [1]. *Journal of the American Chemical Society* **87** (22), 5250–5251 (1965), doi:10.1021/ja00950a048, https://pubs.acs.org/doi/abs/10.1021/ja00950a048.

42. E. Ravera, C. Luchinat, G. Parigi, Basic facts and perspectives of Overhauser DNP NMR. *Journal of Magnetic Resonance* **264**, 78–87 (2016), doi:10.1016/j.jmr.2015.12.013, https://linkinghub.elsevier.com/retrieve/pii/S1090780715003146.

43. D. R. Glenn, *et al.*, High-resolution magnetic resonance spectroscopy using a solid-state spin sensor. *Nature* **555** (7696), 351–354 (2018), doi:10.1038/nature25781, http://www.nature.com/articles/nature25781.

44. D. B. Bucher, D. R. Glenn, H. Park, M. D. Lukin, R. L. Walsworth, Hyperpolarization-Enhanced NMR Spectroscopy with Femtomole Sensitivity Using Quantum Defects in Diamond. *Physical Review X* **10** (2), 021053 (2020), doi:10.1103/PhysRevX.10.021053, https://link.aps.org/doi/10.1103/PhysRevX.10.021053.

45. S. Schmitt, *et al.*, Submillihertz magnetic spectroscopy performed with a nanoscale quantum sensor. *Science* **356** (6340), 832–837 (2017), doi:10.1126/science.aam5532, https://www.sciencemag.org/lookup/doi/10.1126/science.aam5532.

46. N. Niccolai, *et al.*, NMR Studies of Protein Hydration and TEMPOL Accessibility. *Journal of Molecular Biology* **332** (2), 437–447 (2003), doi:10.1016/S0022-2836(03)00852-0, https://linkinghub.elsevier.com/retrieve/pii/S0022283603008520.

47. C. F. Pantoja, A. Ibáñez De Opakua, M. Cima-Omori, M. Zweckstetter, Determining the Physico-Chemical Composition of Biomolecular Condensates from Spatially-Resolved NMR. *Angewandte Chemie International Edition* **62** (17) (2023), publisher: Wiley, doi:10.1002/anie.202218078, https://onlinelibrary.wiley.com/doi/10.1002/anie.202218078.

48. R. W. Tibble, J. D. Gross, A call to order: Examining structured domains in biomolecular condensates. *Journal of Magnetic Resonance* **346**, 107318 (2023), publisher: Elsevier BV, doi:10.1016/j.jmr.2022.107318, https://linkinghub.elsevier.com/retrieve/pii/S1090780722001768.

49. P. Amrein, *et al.*, Optimal bi-planar gradient coil configurations for diamond nitrogen-vacancy based diffusion-weighted NMR experiments. *Magnetic Resonance Materials in Physics, Biology and Medicine* **36** (6), 921–932 (2023), publisher: Springer Science and Business Media LLC, doi:10.1007/s10334-023-01111-0, https://link.springer.com/10.1007/s10334-023-01111-0.

50. V. Moxley-Paquette, *et al.*, Development of Low-Magnetic Susceptibility Microcoils via 5-Axis Machining for Analysis of Biological and Environmental Samples. *Analytical Chemistry* **95** (37), 13932–13940 (2023), doi:10.1021/acs.analchem.3c02437, https://pubs.acs.org/doi/10.1021/acs.analchem.3c02437.

51. H. Ryan, A. Smith, M. Utz, Structural shimming for high-resolution nuclear magnetic resonance spectroscopy in lab-on-a-chip devices. *Lab Chip* **14** (10), 1678–1685 (2014), doi:10.1039/C3LC51431E, https://xlink.rsc.org/?DOI=C3LC51431E.

52. C. Munuera-Javaloy, A. Tobalina, J. Casanova, High-Resolution NMR Spectroscopy at Large Fields with Nitrogen Vacancy Centers. *Physical Review Letters* **130** (13), 133603 (2023), doi:10.1103/PhysRevLett.130.133603, https://link.aps.org/doi/10.1103/PhysRevLett.130.133603.

53. J. Eills, M. W. Mitchell, I. M. Rius, M. C. D. Tayler, Live magnetic observation of parahydrogen hyperpolarization dynamics. *Proceedings of the National Academy of Sciences* **121** (43) (2024), publisher: Proceedings of the National Academy of Sciences, doi:10.1073/pnas.2410209121, https://pnas.org/doi/10.1073/pnas.2410209121.

54. F. Bruckmaier, K. D. Briegel, D. B. Bucher, Geometry dependence of micron-scale NMR signals on NV-diamond chips. *Journal of Magnetic Resonance Open* **8-9**, 100023 (2021), doi:10.1016/j.jmro.2021.100023, https://linkinghub.elsevier.com/retrieve/pii/S2666441021000145.

55. N. Arunkumar, *et al.*, Quantum Logic Enhanced Sensing in Solid-State Spin Ensembles. *Physical Review Letters* **131** (10), 100801 (2023), doi:10.1103/PhysRevLett.131.100801, https://link.aps.org/doi/10.1103/PhysRevLett.131.100801.

56. A. Berzins, *et al.*, Impact of microwave phase noise on diamond quantum sensing. *Physical Review Research* **6** (4), 043148 (2024), doi:10.1103/PhysRevResearch.6.043148, https://link.aps.org/doi/10.1103/PhysRevResearch.6.043148.

57. H. Zhou, *et al.*, Robust Higher-Order Hamiltonian Engineering for Quantum Sensing with Strongly Interacting Systems. *Physical Review Letters* **131** (22), 220803 (2023), doi:10.1103/PhysRevLett.131.220803, https://link.aps.org/doi/10.1103/PhysRevLett.131.220803.

58. J. Zhang, *et al.*, Learning to steer quantum many-body dynamics with tree optimization (2025), doi:10.48550/arXiv.2510.07802, http://arxiv.org/abs/2510.07802, arXiv:2510.07802 [quant-ph].

59. M. C. Wapler, *et al.*, Magnetic properties of materials for MR engineering, micro-MR and beyond. *Journal of Magnetic Resonance* **242**, 233–242 (2014), doi:10.1016/j.jmr.2014.02.005, https://linkinghub.elsevier.com/retrieve/pii/S1090780714000433.

Acknowledgments

We thank Dominik Bucher and Ruoming Peng for the technical advice and fruitful discussion. We thank Yunyu Shi for the enlightening discussion on liquid-liquid phase separation. We thank Element Six for providing the diamond sample. Device fabrication was partially carried out at the USTC Center for Micro- and Nanoscale Research and Fabrication.

Funding: This work was supported by the National Natural Science Foundation of China (grant no. T2125011), the Chinese Academy of Sciences (grant no. YSBR-068), Innovation Program for Quantum Science and Technology (Grant No. 2021ZD0302200, 2021ZD0303204), New Cornerstone Science Foundation through the XPLORER PRIZE, and the Fundamental Research Funds for the Central Universities.

Author contributions: J.D. and F.S. supervised the project and proposed the idea. F.S., M.S., S.X., and J.D. designed the experiments. M.S. and X.K. prepared the setup and built the experiment software. M.S., Q.R., and S.X. prepared the protein samples. M.S., Z.Z., and T.X. performed the data acquisition and visualization in the experiment. M.S., F.S., S.X., and J.D. wrote the manuscript. All authors analysed the data, discussed the results, and commented on the manuscript.

Competing interests: There are no competing interests to declare.

Data and materials availability: All data needed to evaluate the conclusions in the paper are present in the paper and/or the Supplementary Materials.

Supplementary materials

Supplementary Materials for Chemically Resolving Protein Phase Separation with Quantum-Enhanced Picoliter NMR

Mengze Shen[1†], Zhiyuan Zhao[1,2†], Haolin Zhang[1,2], Qiunan Ren[3], Xi Kong[8], Zhiping Yang[1,2,5], Tianyu Xie[1,2], Ke Ruan[1], Shengqi Xiang[1,3*], Fazhan Shi[1,2,4,5,6*], Jiangfeng Du[4,7*]

[*]Corresponding author. Email: fzshi@ustc.edu.cn, cqxiang@ustc.edu.cn, djf@ustc.edu.cn

[†]These authors contributed equally to this work.

This PDF file includes:

Materials and Methods

NV ensemble sensor

The nitrogen-vacancy (NV) center is a stable point defect in diamond, formed by a nitrogen atom and an adjacent vacancy in the diamond's lattice. This defect possesses an electronic spin with ground-state sublevels denoted as $m_s = 0$ and $m_s = \pm 1$. The energy gap between these sublevels is sensitive to external magnetic fields, including the faint, oscillating field produced by nuclear spins in a nearby sample, which is the basis of an NMR signal.

The key to the NV-NMR protocol is the ability to optically read out the NV center's spin state. The NV's fluorescence intensity under green laser illumination exhibits spin dependence: the $m_s = 0$ state is significantly brighter than the $m_s = \pm 1$ states. By applying a microwave field, we can drive transitions between these states. When the microwave frequency resonates with the energy gap (which is shifted by the NMR signal), the NV population is transferred from the bright $m_s = 0$ state to the dimmer $m_s = \pm 1$ states, causing a detectable drop in the measured fluorescence. This optically detected magnetic resonance (ODMR) technique effectively converts a weak magnetic NMR signal into a high-contrast optical signal, which enables higher sensitivity detection.

Our specific NV ensemble sensor is based on a 3.6 mm × 3.6 mm × 0.5 mm diamond chip with the top face perpendicular to the [100] crystal axis. The diamond is made by chemical vapor deposition (CVD) with 99.999% ^{12}C isotopic purity with a bulk nitrogen concentration of $[^{14}\mathrm{N}] < 8.8 \times 10^{14}\mathrm{cm}^{-3}$. In the final stage of CVD, a 10 μm-thick NV layer is grown on the surface, with a nitrogen concentration of $[^{14}\mathrm{N}] \approx 1.9 \times 10^{18}\mathrm{cm}^{-3}$. After electron irradiation and annealing, it forms a layer with NV concentration $[\mathrm{NV}] \approx 7 \times 10^{17}\mathrm{cm}^{-3}$. The decoherence of the NV ensemble is $T_2 \approx 10$ μs with the Hahn echo and $T_2^* \approx 1$ μs with the Ramsey measurement.

Protein Sample

The preparation of the protein sample in this experiment is listed as follows:

1. **Protein Construct**

   The GLH-1 FGG region (residues 15-154) was constructed in vector pET-28a via homologous recombination with an N-terminal His-SUMO tag for purification. The recombinant protein was expressed in the *Escherichia coli* strain BL21.

2. **Expression and Purification**

   Bacterial cells were grown in Luria broth media, induced at OD_{600} = 0.8 at 37 °C, and harvested 5 h later by centrifugation at 4500 g for 15 min. The cell pellet was resuspended in buffer A (25 mM HEPES, pH 7.0, and 500 mM NaCl), lysed by a high-pressure cell crusher, and then centrifuged at 19000 g for 30 min. The supernatant was purified via a Ni-NTA affinity column. The bound GLH-1 FGG proteins were washed with buffer B (25 mM HEPES, 500 mM NaCl, 25 mM imidazole, pH 7.0) and then eluted from the column with an elution buffer C (25 mM HEPES, 500 mM NaCl, 500 mM imidazole, pH 7.0). Then, the His-SUMO tag was cleaved by Ulp1 protease, and the protein was dialyzed against 25 mM NaH_2PO_4, pH 7.0, and 150 mM NaCl at 4 °C. The proteins were again loaded onto the Ni-NTA column to remove the Ulp1 protease and His-SUMO-tag.

3. **Phase Separation Sample Collection**

   The protein solution was dialyzed sequentially against buffers containing decreasing salt concentrations (100 mM → 50 mM → 20 mM) using 3.5 kDa MWCO tubing at 4 °C. Then, the protein solution was concentrated to 4 mg/mL using a 5 kDa MWCO centrifugal concentrator (Sartorius Vivaspin) and subsequently lyophilized. For the final NMR sample, the lyophilized protein powder was redissolved in D_2O (0.3 mL) and mixed with a stock solution of TEMPOL. This yielded the final sample ready for analysis, containing approximately 2.6 mM protein and 10 mM TEMPOL, which spontaneously undergoes phase separation. At the concentration used, TEMPOL induces no significant changes to the protein's NMR spectrum (*46*). Deuterium oxide (D_2O, 99.9 atom % D) and TEMPOL (4-Oxo-TEMPO) were purchased from Manalab and Sigma-Aldrich, respectively.

Conventional ^{1}H NMR Reference Spectroscopy

The one-dimensional ^{1}H NMR spectrum of the purified GLH-1 FGG fragment was acquired to act as a reference for the NV-detected data presented in the main text (Fig. 3C). An exponential apodization was applied to the original spectrum to broaden the resolution to 0.33 ppm, which matches the resolution of NV-NMR for comparison. For the conventional NMR reference measurement, the sample was prepared identically to the one used for the NV-NMR experiment, to ensure

a direct comparison between the two modalities. The spectrum was recorded on a 600 MHz liquid-state NMR spectrometer (JNM-ECZ600R/S1) at room temperature. The spectrum consisted of 128 scans. 32,768 data points were collected for each scan with 20 ppm spectral width. The baseline adjustment and the line broadening in the main text were automatically performed by MestReNova (Mestrelab Research, Spain).

Experimental protocols and data analysis

The 532 nm laser is generated by a diode-pumped solid-state laser (Lighthouse Sprout-D-5W), then it is pulsed by an acousto-optic modulator (Brimrose TEM-85-10-532) driven by a manufacturer-supplied driver module. The estimated power of the laser reaching the diamond is ~120 mW. Considering the 30 μm spot and the reflective film on the surface, the power intensity is around 34 kW/cm^2.

For optical detection, fluorescence is collected by a CPC lens (Edmunds Optics) and goes to a photodiode (Thorlabs PDAPC2) behind a 650-nm long-pass filter (Thorlabs FELH0650). The estimated power of the collected fluorescence is ~160 μW, calculated by a photocurrent around ~80 μA. The output voltage of photodiodes is recorded with a digital-to-analogue converter (DAQ) (CIQTEK DAQ2100). The DAQ sampling rate is 1 GHz, and it is triggered by a transistor–transistor logic (TTL) pulse from the arbitrary-sequence generator (ASG) (CIQTEK CRS) in sequences. In each readout, the laser was first turned on for 1 μs to initialize NV centers, and then 2.048 μs for the fluorescence readout, followed by a 6 μs pulse to fully repolarize the NV centers, ensuring optimized contrast. Laser intensity noise was suppressed using a balanced detection scheme. A second, identical photodiode monitored the laser output, allowing for common-mode rejection of intensity fluctuations. Before measurements, the electronic offsets of both detectors were nulled in the dark.

The entire experimental sequence was controlled by the ASG (CIQTEK CRS), with all devices synchronized to a common 10 MHz clock from a Keysight 33522B AWG. Each measurement cycle began with a 150 ms Overhauser dynamic nuclear polarization (ODNP) pulse to enhance the NMR signal; this was driven by a 3.41 GHz microwave pulse from a Rigol DSG3065B signal generator. Subsequently, a 250 μs nuclear $\pi/2$ pulse at ~5.19 MHz was applied to excite the nuclear spins, generated by a Keysight 33522B AWG and amplified by an RF amplifier (Mini-

circuits LZY-22+). The resulting free induction decay (FID) signal was detected using a coherently averaged synchronized readout (CASR) sequence composed of XY16-12 dynamical decoupling (DD) blocks. Microwave pulses at 544 MHz, corresponding to the resonance under a bias magnetic field of $B_0 = 121.8$ mT, were generated by a Keysight M8190 AWG. These pulses were used to drive the $|m_s = 0\rangle \rightarrow |m_s = -1\rangle$ spin transition of aligned NV centers during the DD sequence. Both the ODNP and NV drive microwaves were combined and amplified by a Mini-circuits amplifier (ZHL-25-63+). For noise cancellation, the interval between two sub-sequences was set to $(n + 0.5) \times 1/f_{\mathrm{Larmor}}$, and the contrast of each data point was calculated by subtracting two consecutive readouts and normalized by the average of two readouts. The detailed timing parameters for the DD sequence were an inter-pulse delay $\tau = 96.33$ ns, an NV $\pi/2$-pulse of $t_{\pi/2,\mathrm{NV}} = 34.25$ ns, and an NV π-pulse of $t_{\pi,\mathrm{NV}} = 69.75$ ns, resulting in a total DD sub-sequence length of ~20 μs.

All time-domain NMR data were processed using a consistent workflow. First, the initial 0.3 ms of the signal (the first 4 data points) was discarded to exclude transient effects from incomplete NV spin polarization. Subsequently, a mild high-pass filter was applied to remove low-frequency baseline drift by subtracting a moving average from the time-domain data. The filtered data were then converted to the frequency domain via a Fast Fourier Transform (FFT). Specific processing parameters varied slightly for each experiment:

- Benchmark Spectrum (Fig. 1C to F): Time-domain data from single-shot measurements were baseline-corrected using a 90 ms (1200 points) moving average window, followed by zero-padding to 1800 ms (24,000 points) before the FFT. The resulting frequency-domain spectrum was manually phase-corrected, and the real part was plotted to yield the final spectrum.

- Protein Spectrum (Fig. 2C, Fig. 3B): Each spectrum was obtained by averaging 1300 individual measurements. To compensate for slow magnetic field drifts, the Larmor frequency for each acquisition was corrected based on an ODMR measurement performed immediately before the main NMR sequence. The averaged time-domain data were processed as follows: first, a mild high-pass filter was applied by subtracting a moving average with a 40-ms (600 points) window to correct for baseline drift. Subsequently, an exponential window function (apodization) with a time constant of $\lambda = 300$ ms was applied to enhance the signal-to-noise ratio. Finally, the data were zero-padded to ~1600 ms (24,000 points) before the FFT. Due

to the low signal-to-noise ratio and complex, overlapping line shapes of the protein signals, consistent manual phase correction was not feasible. Therefore, the magnitude spectrum was calculated and displayed.

- Blank Control Spectrum (Fig. 2A, B, D): Spectra in panels A, B, and D were obtained from 20, 400, and 1000 averages, respectively. The settings for baseline correction, apodization, and zero-padding were identical to those used for the protein spectrum.

The chemical shift axis of the NV-detected spectrum was calibrated against the conventional NMR spectrum of the same sample. Due to the significant magnetic susceptibility effects at the diamond-sample interface, which make absolute chemical shift determination difficult, we aligned the prominent signal clusters of the NV-detected spectrum to the corresponding fingerprint pattern in the conventional NMR spectra (Fig. 3C). This procedure allows for a direct comparison of the relative peak positions and spectral patterns between the two methods.

Resulting spectral peaks were analyzed by fitting to a Lorentzian lineshape function. The extracted parameters for the three main protein peaks—center position (x_c), width (w), and area (A)—are reported as values ± standard error (in ppm) in Table S1. All data processing, analysis, and plotting were performed using Origin 2023b (OriginLab Corp., USA) and MATLAB R2024a (MathWorks Inc., USA). Additionally, the schematic illustration of the NV center (Fig. 1A inset) was rendered in Blender (Blender Foundation), and the final figure layout was assembled in Inkscape (The Inkscape Project).

Supplementary Text

Generation of Homogeneous Stable Magnetic Field

The static bias magnetic field was generated by an H-frame samarium-cobalt magnet with a 54 mm gap between its pole pieces and a field of 121.8 mT (figure S3). To enhance the field homogeneity across the sensing volume, passive shimming was performed by affixing multiple magnetic beads of various sizes at different locations on the pole faces. The entire magnet assembly was wrapped in thermal insulation foam to mitigate field drifts arising from ambient temperature fluctuations. For active field stabilization, a pair of Helmholtz coils was mounted on the pole pieces, providing a

feedback field response of 0.55 Gs/V. The magnet was mounted on a custom-built 5-axis stage (main components from BOCIC), with x, y, z translation and two rotational (tip/tilt) axes, for aligning the magnetic fields to the axis of NV and placing the sensing area in the center of the magnet.

Our platform operates in a complex magnetic environment, characterized by both fast-changing spatial noise and slow field drifts from magnet temperature changes. Therefore, our experiment employs a dual-stage feedback system—utilizing two distinct sensors and a pair of Helmholtz coils—to simultaneously suppress these two distinct noise effects and ensure magnetic field stability: (i) An asynchronous feedback loop continuously cancels fast, high-amplitude environmental noise (e.g., from urban sources). This is achieved using an external fluxgate sensor (Witmotion HWT-3100) that monitors the ambient field and applies a real-time correction. (ii) A synchronous feedback loop corrects for slower internal drifts, such as those caused by thermal fluctuations. By analyzing the ODMR spectrum from the same NV centers before each of the NMR measurement sequences, the precise magnetic field has been recorded synchronously with each of the main NMR acquisition datasets. This hybrid feedback strategy ensures the necessary field stability for long-duration measurements without requiring magnetic shielding.

Reflective Film Pattern

A metallic reflective pattern was fabricated on the diamond surface to shield the protein sample from laser illumination. The fabrication was performed using a shadow mask workflow (Fig. S4). First, a 50-μm-thick polydimethylsiloxane (PDMS) mask containing an array of micro-wells was covered on the diamond surface. The diamond and mask assembly was then mounted in an electron beam evaporator for metal deposition. The filming rate of Ti/Ag/Al is approximately 0.02 $nm \cdot s^{-1}$/0.08 $nm \cdot s^{-1}$/0.08 $nm \cdot s^{-1}$. Following deposition, the PDMS mask was carefully removed, leaving an array of discrete, reflective metal patterns on the diamond's surface. Subsequently, one of these patterns was aligned with the center of the coil on the PCB. The reflective film serves a dual purpose: it enhances the collection efficiency of the NV fluorescence while improving the signal contrast by blocking background fluorescence from the underlying PCB.

Preparation of PCB-Microfluids Structure

The microwave control structure was fabricated on a 100 μm-thick flexible Taconic TLY-5 printed circuit board (PCB) substrate with a 17 μm-thick (1/2 Oz.) copper layer. The Taconic TYL-5 laminate is constructed from woven glass fabric coated in PTFE that is embedded with pure PTFE flakes. Both copper and PTFE share a similar magnetic susceptibility with water solution (*59*). The surface of the copper was protected with a layer of immersion silver. The microfluidic channel, with nominal dimensions of approximately 200 μm × 200 μm (width × height), was created by wet etching a straight channel into a glass chip. This channel serves to connect the fluidic input and output to the ports on the PCB. The two components were integrated to form the final sensing device. The PCB and the etched glass chip were bonded together using a UV-curable adhesive to prevent leakage. The diamond chip, with its patterned side facing the channel, was then mounted on the opposite side of the PCB and sealed with wax. During this process, a single reflective metal pattern was aligned to the center of the microfluidic channel, defining the final, confined sample detection volume. Finally, an 8-turn, single-layer concentric copper coil is mounted on the back side of the glass channel. This coil generates the radiofrequency (RF) pulses required to manipulate nuclear spins during the NMR experiment. The inner and outer diameters of the coil are 3 mm and 5 mm with a wire diameter of 80 μm.

Workflow of loading protein sample

To ensure that the detected NMR signals originated predominantly from the protein sample and not from residual solvent protons, a rigorous, multi-step sample loading procedure was implemented. First, the microfluidic channel was thoroughly flushed with D_2O to remove any residual H_2O from the system. Following this initial flush, a background NMR experiment was performed to verify the absence of a significant water signal. This step served as a critical quality control check. If a residual H_2O signal was detected, the D_2O flushing and background NMR acquisition cycle was repeated iteratively until the solvent signal was reduced to a negligible level. Only after confirming a clean, proton-free background was the prepared protein sample injected into the microfluidic channel for the definitive NMR experiment. This workflow, which replaces complex water-suppression pulse sequences, ensures the resulting spectrum is a clear representation of the protein sample.

Strong Coupling Effects at Low Field

At the operating magnetic field of our NV-NMR setup (~121.8 mT), the Larmor frequency is approximately 5.19 MHz. Consequently, the chemical shift difference ($\Delta\delta$) between protons is often comparable to or smaller than their scalar coupling constants (J), placing the system in the strong coupling regime. This leads to second-order spectral effects, such as the "roof effect" and mixing of spin states, which can distort peak shapes and broaden signal linewidths. However, the comparison with high-field NMR spectra (Fig. 3C) remains valid for two key reasons. First, the dominant signal at ~3.8 ppm originates from Glycine (~53% of the sequence). Since Glycine lacks a side chain, its α-protons constitute an isolated spin system that does not scalar couple to the upfield side-chain protons (mainly at ~3.0 ppm). This ensures that the two primary signal clusters remain chemically distinct without mixing. Second, quantum mechanics dictates that the first spectral moment (center of gravity) of a coupled spin system is conserved at the average chemical shift, regardless of the coupling strength. Since the high-field reference spectrum was exponentially broadened to match the NV-NMR linewidth (~0.33 ppm), removing fine scalar coupling structures, the comparison of the signal envelopes and their relative positions remains valid.

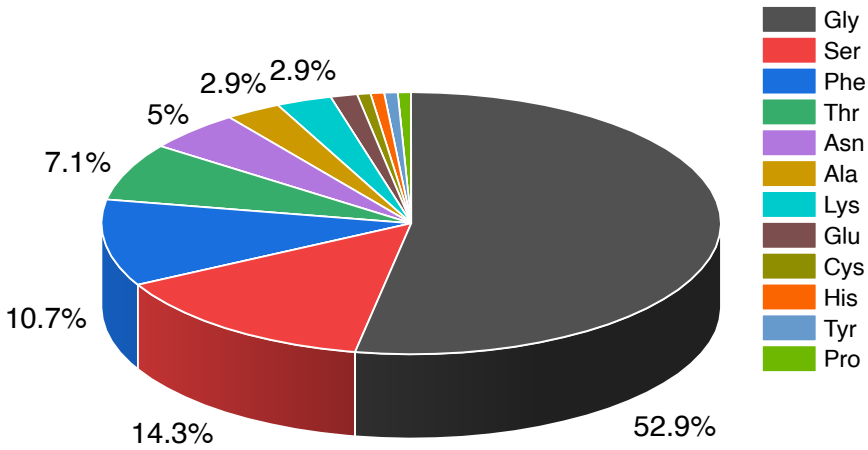

Figure S1: **Amino acid composition of the GLH-1 FGG (15-154) protein sample.**This pie chart illustrates the relative abundance (in percentage) of each amino acid residue within the studied GLH-1 FGG region (residues 15-154). The analysis highlights the high abundance of Glycine (Gly, 52.9%), Serine (Ser, 14.3%), and Phenylalanine (Phe, 10.7%). These three amino acids collectively constitute over 75% of the total residues. This compositional analysis provides the basis for assigning the prominent signal clusters observed in the main text's NMR result (Fig. 3).

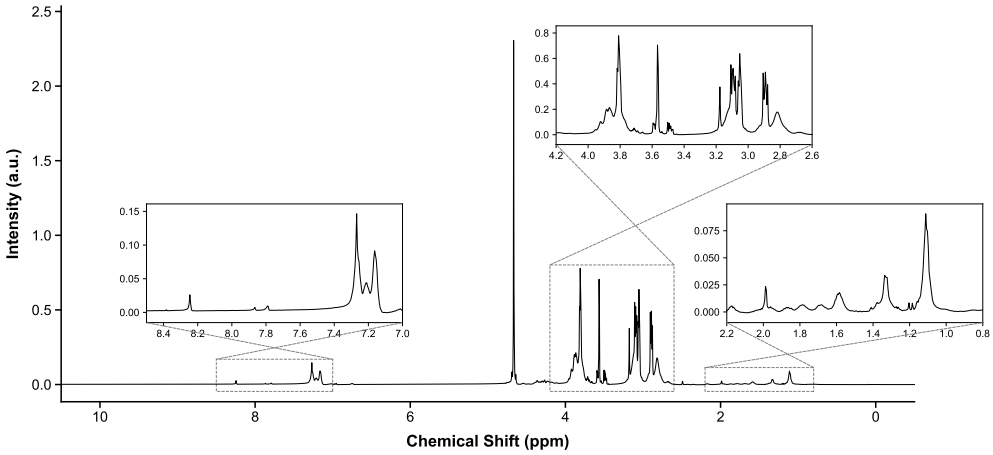

Figure S2: **Conventional ^{1}H NMR spectrum of the GLH-1 FGG fragment in D_2O.** This one-dimensional ^{1}H NMR spectrum was acquired to be a high-resolution reference for the NV-detected data presented in the main text (Fig. 3C). To ensure a direct comparison, the sample was prepared identically to the one used for the NV-NMR experiment. The spectrum was recorded on a 600 MHz liquid-state NMR spectrometer at room temperature. The main panel displays the full spectral range, while the insets provide magnified views of key regions to highlight the detailed peak structures: the aromatic region (7.0-8.4 ppm, left), the α-proton and side-chain region (2.8-4.2 ppm, top), and the upfield aliphatic region (0.8-2.2 ppm, right).

Table S1: **Lorentzian fitting parameters for the main signal peaks.** The table lists parameters for the three main signal peaks observed in the NV-detected NMR spectrum. The peak labels correspond to those used for the deconvolution in Fig. 3B. Values are reported as mean ± standard error.

Peak	**Center, x_c (ppm)**	**Width, w (ppm)**	**Area, A (a.u. $\times 10^{-6}$)**
1	2.975 ± 0.029	0.343 ± 0.087	1.843 ± 0.403
2	3.668 ± 0.041	0.487 ± 0.143	2.187 ± 0.519
3	4.749 ± 0.037	0.346 ± 0.116	1.353 ± 0.328

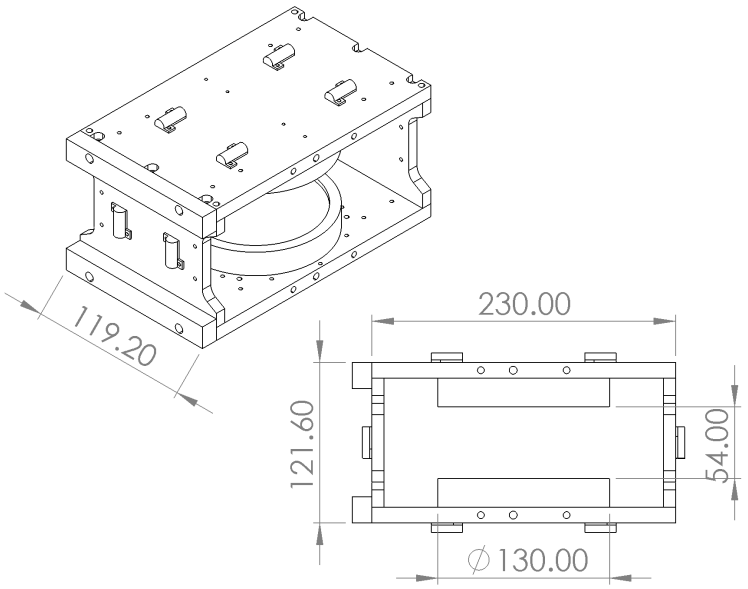

Figure S3: **Technical drawing of the H-frame permanent magnet.** This schematic provides the technical drawing for the H-frame permanent magnet used to generate the static bias magnetic field (B_0 = 121.8 mT) for the NMR experiments. The figure displays both an isometric view (top left) and an orthographic view (bottom right) of the magnet assembly. Key dimensions are indicated, including the 54 mm gap between the pole pieces where the sample is placed. All dimensions shown are in millimeters. The total weight of the magnets is approximately 16 kg.

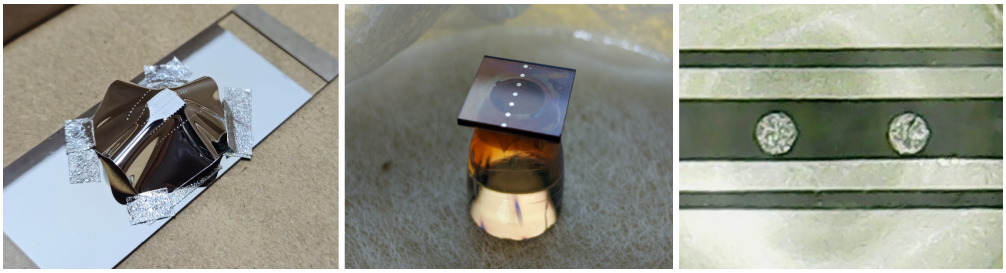

Figure S4: **Fabrication workflow for the patterned reflective film on the diamond surface.** These photographs illustrate the shadow mask workflow used to create discrete, reflective metal patterns on the diamond surface. The purpose of this patterned geometry is to shield the biological sample from laser illumination while minimizing perturbation of the microwave field required for spin manipulation. **(Left)** A polydimethylsiloxane (PDMS) shadow mask with an array of micro-wells is placed onto the diamond surface before metal deposition. **(Middle)** The diamond chip after the deposition of the Ti/Ag/Al reflective film and subsequent removal of the PDMS mask, showing the resulting array of metallic patterns. **(Right)** A microscope image of two of the final circular reflective patterns on the diamond. During assembly, one such pattern is aligned with the microfluidic channel formed by a parallel coil.